Effects of Dynamical Capture on two equal-mass non-spinning black holes

Jorge L. Rodríguez-Monteverde,^{1,*} Santiago Jaraba,^{2,†} and Juan García-Bellido^{3,‡}

¹ Universidad Autónoma de Madrid, Cantoblanco 28049 Madrid, Spain

² Observatoire astronomique de Strasbourg, CNRS,

Université de Strasbourg, 11 rue de l'Université, 67000 Strasbourg, France

³ Instituto de Física Teórica UAM-CSIC, Universidad Autónoma de Madrid, Cantoblanco 28049 Madrid, Spain

(Dated: October 23, 2025)

Abstract

Dynamical captures of black holes are unique events that provide an exceptional opportunity to probe the strong-field regime of gravitational physics. In this article, we perform numerical relativity simulations to study the events of dynamical capture of two equal-mass non-spinning black holes. We consider a suite of scenarios within a range of initial linear momenta (p/M=0.095-0.75) and incidence angles $(\theta=6.36^{\circ}-2.83^{\circ})$, and study the emitted Weyl scalar (Ψ_4) of each case, as well as the spins and masses of the black holes before and after they merge. We provide a simple analytical model which accurately fits the gravitational-wave emission. We study the dependence of the time-interval between the capture and the merger emissions with respect to the incidence angle, which can be well parametrized by a first-order divergent behavior, allowing to find the angle that separates a scattering event from a dynamical capture. We also find that, in general, the parameters that model the first emission can be well described by linear or exponentially decaying functions in terms of the incidence angle, while others display more complex behaviors that offer valuable insights into the nature of these events.

I. INTRODUCTION

Dynamical capture (DC) and close hyperbolic encounters (CHEs) of black holes (BHs) have recently gained increasing attention as key processes in dense astrophysical environments. CHEs, in particular, are of growing interest due to their potential implications for the dynamics and evolution of primordial black holes (PBHs) in dense clusters [1–8]. On the other hand, a DC can be understood as the limiting case in which a hyperbolic encounter radiates sufficient energy and angular momentum through gravitational waves (GWs) to bind two initially unbound BHs into a merging system. Together with pure scattering events, these scenarios are expected to play a central role in the dynamics of BH clusters, influencing their long-term evolution and the properties of the gravitational wave signals they generate [9–11].

Accurately modeling these interactions is crucial for the development of precise N-body simulations of dense BH clusters. Such simulations will allow us to predict the resulting mass and spin distributions of black holes and assess the detectability of the GWs they produce [12]. However, the observational prospects for identifying DC events with current ground-based detectors such as those of the LIGO-Virgo-KAGRA (LVK) Collaboration [13–15] remain limited. Detectability is hampered by the requirement of long-duration measurements and high-precision sensitivity. Nonetheless, as detector sensitivity improves, it is plausible that DC signatures may be identified in LVK [10, 16, 17]. In fact, the event GW190521 was proposed as being the first detection of a GW signal coming from a dynamical capture of non-

spinning black holes, preferred over a quasi-circular spinprecessing merger [18].

In this work, we use Numerical Relativity (NR) to run simulations of initially non-spinning, equal-mass black holes ($q \equiv m_2/m_1 = 1$). We leave the inclusion of spin and mass-ratio asymmetries to future studies. This choice is motivated by the expectation that PBHs form with low initial spins [19], with their angular momenta subsequently altered through repeated dynamical interactions, most prominently via CHEs, as shown in previous studies [3, 4, 7].

This paper is organized as follows: in Sec. II we present some basic theoretical aspects that will be relevant for our discussion, we also describe the numerical setup we use and our choice of initial conditions; in Sec. III we discuss the general behavior of our simulations, the concrete details of the used waveform model and we show the results this phenomenological model provides; in Sec. IV we analyze many relevant properties related to the mass and spin of the initial and final black holes; and lastly, in Sec. V we summarize our findings and outline future directions.

Finally, the results in this work will be presented using geometrized units, G=c=1, the usual convention for NR simulations.

II. PRELIMINARY FRAMEWORK

To properly discuss the phenomenology that arises from dynamical captures, we must first introduce some fundamental aspects that are necessary to understand and build a DC of BHs simulation. Firstly, we briefly present some theoretical aspects such as the outgoing gravitational radiation, the black hole apparent horizons and the measuremt of BH spins; and secondly, we introduce the numerical framework: the grid setup, the general initial BH configuration and the selection of initial

^{*} jorge.lopezr@estudiante.uam.es

 $^{^{\}dagger}$ santiago.jaraba-gomez@astro.unistra.fr

[‡] juan.garciabellido@uam.es

conditions used in our simulations.

A. Weyl scalar

Gravitational-wave radiation can be extracted from the *Newman-Penrose formalism* via the Weyl scalar Ψ_4 , which encodes the outgoing gravitational radiation in terms of a null tetrad basis [20, 21]:

$$\Psi_4 = C_{\mu\nu\rho\sigma} \, n^\mu \overline{m}^\nu n^\rho \overline{m}^\sigma, \tag{1}$$

where $C_{\mu\nu\rho\sigma}$ is the Weyl tensor, n^{μ} is one of the null basis vectors, and \overline{m}^{μ} is the complex conjugate of the corresponding tetrad vector m^{μ} .

The quantity Ψ_4 captures the curvature perturbations associated with outgoing gravitational radiation and is directly related to the observable gravitational-wave strain. The complex combination of the two polarization states, h_+ and h_\times , can be obtained from Ψ_4 through a double time integration:

$$h_{+}(\vec{x},t) - ih_{\times}(\vec{x},t) = \int_{-\infty}^{t} du \int_{-\infty}^{u} dv \, \Psi_{4}(\vec{x},v),$$
 (2)

where both the strain components and the Weyl scalar can be expanded in terms of their spherical harmonic modes in the following manner:

$$h_{+,\times}(\vec{x},t) = \sum_{l=2}^{\infty} \sum_{m=-l}^{+l} h_{+,\times}^{lm}(r,t) Y_{-2}^{lm}(\theta,\phi).$$
 (3)

In practice, extracting the quantity Ψ_4 from NR simulations provides a robust and gauge-invariant measure of gravitational radiation. For both clarity and numerical accuracy, our analysis focuses on the dominant quadrupolar mode, $\Psi_4^{(2,2)}$, which typically carries the majority of the emitted energy in binary black hole (BBH) coalescences.

B. Apparent horizons

The identification of BH horizons plays a central role in accurately describing the dynamics of the full BBH system within a NR simulation. In dynamical spacetimes, however, the event horizon (the null hypersurface that defines the boundary of the BH region of a spacetime) is a global property. This makes it impractical for real-time numerical tracking, since its location depends on the entire future evolution of the spacetime.

Instead, apparent horizons provide a local and physically meaningful notion of a black hole boundary during dynamical evolution. An apparent horizon is defined as a closed two-surface where the expansion of outgoing null geodesics vanishes, i.e., a surface that locally separates outgoing and ingoing light rays. Mathematically, it satisfies

$$q^{ij}(K_{ij} - D_i s_j) = 0, (4)$$

where s_i is the spacelike unit normal to the horizon surface, D_i denotes the covariant derivative compatible with the spatial metric γ_{ij} , $q_{ij} = \gamma_{ij} - s_i s_j$ is the induced two-metric on the surface, and K_{ij} is the extrinsic curvature [22].

Once the apparent horizon is located, its area A can be computed, which in turn allows one to define the horizon mass [23]:

$$m_H = \sqrt{\frac{A}{16\pi} + \frac{4\pi J^2}{A}},$$
 (5)

where J is the angular momentum of the black hole.

To interpret this relation, it is convenient to introduce two key mass definitions. The ADM (or horizon) mass, $m \equiv m_H$, represents the total energy content of the isolated system in an asymptotically flat spacetime. The irreducible mass,

$$m_{\rm irr} \equiv \sqrt{\frac{A}{16\pi}},$$
 (6)

corresponds to the portion of the black hole's mass that cannot be reduced by any classical process, even those capable of extracting rotational energy (such as the Penrose process or black hole mergers) [24].

In terms of these quantities, Eq. (5) can be rewritten as

$$m_H = \sqrt{m_{\rm irr}^2 + \frac{J^2}{4m_{\rm irr}^2}},$$
 (7)

which elegantly expresses the total black hole mass as the sum of its irreducible (non-extractable) and rotational energy contributions.

C. Measuring spin

The spin of a black hole in a dynamical spacetime is a gauge-dependent quantity, and therefore admits several distinct definitions. Only in the limit where BHs are well separated and approximately stationary do all spin measures coincide. One of the most practical ways to estimate BH spins in NR simulations is through the geometric properties of their apparent horizons.

The spin can be inferred from the shape of the apparent horizon via the relation [25]:

$$\frac{C_p}{C_e} = \frac{1 + \sqrt{1 - \chi^2}}{\pi} E\left(-\frac{\chi^2}{(1 + \sqrt{1 - \chi^2})^2}\right), \quad (8)$$

where C_p and C_e denote the polar and equatorial circumferences (measured along their respective geodesics), $\chi = a/m = J/m^2$ is the dimensionless spin parameter (more thoroughly defined in previous references such as [4, 7, 26]), and E(x) is the complete elliptic integral of the second kind, defined as

$$E(x) = \int_0^{\pi/2} d\theta \sqrt{1 - x \sin^2 \theta}.$$
 (9)

In our simulations, this computation is performed automatically by the QuasiLocalMeasures thorn [27], which provides a consistent framework for evaluating quasi-local quantities such as mass, spin, and angular momentum directly from the horizon geometry.

D. Grid properties and initial black hole configuration

The simulations were performed using the Einstein Toolkit [28, 29]. In particular, we employed the Cactus Computational Toolkit [30, 31] as the core infrastructure, with adaptive mesh refinement (AMR) handled by Carpet [32, 33]. The initial puncture data were generated using TwoPunctures [34, 35], and the spacetime evolution was carried out using the BSSN formulation implemented in McLachlan [36–38]. To track the apparent horizons, we utilized the AHFinderDirect thorn [39, 40], while the QuasiLocalMeasures thorn [27] was used to compute black hole spins. Lastly, the Weyl scalar Ψ_4 , used for gravitational-wave extraction, was obtained through the WeylScal4 thorn [41].

The initial setup of our simulations is identical to that described in the first sections of [4]. This means we consider equal-mass binary black holes, $m_1 = m_2 \equiv m$, with symmetric linear momenta, $|\vec{p_1}| = |\vec{p_2}| \equiv p$, as well as no spins, $\vec{S_1} = \vec{S_2} = 0$. Working in geometrized units, all quantities such as length, time, and momentum are expressed in units of mass. As is standard in Numerical Relativity, we fix the total mass $M \equiv m_1 + m_2 = 2m = 1$ in the simulations. Therefore, results for a generic total mass M can be obtained by rescaling the dimensionless quantities, which are presented as t/M, p/M, x/M, etc. Working in these units and following the literature, the initial distance between the BHs has been set to d = 100M.

Regarding the computational setup, we follow the same grid configuration as in [3, 4, 7]. The grid hierarchy consists of refinement levels with half-lengths of 0.75×2^n for $n = 0, 1, \ldots, 6, 8, 9, 10$, and grid spacings of $2^n \times \Delta x_{mr}$ for $n = 0, 1, \ldots, 9$, where Δx_{mr} denotes the resolution of the finest grid. In our simulations, we employ a single resolution, $\Delta x_{mr} = (3/200)M$, which in previous works was referred to as medium resolution [4, 7].

Based on these references, and on explicit cross-checks performed here, we find that (with regards to the induced spins) differences between the resolution used here and higher ones remain below 0.6%. Other relevant variables have also been checked to have good accuracy with differences below 1%. Given that the maximum induced spins in our non-spinning case reach only $\chi \sim 0.14$ (in agreement with previous results [7]) we conclude that medium resolution is sufficient to obtain accurate and robust results. Nevertheless, in some simulations dealing with highly relativistic initial conditions (more specifically p/M = 0.75), the formed BH after the merger was observed to have large discrepancies in their masses and

spins, which is the reason we discarded these concrete values for these simulations, as we will indicate in Sec. IV.

E. Choice of initial conditions

We perform a series of simulations using the same setup as in [4], considering equal-mass binaries. The values of the dimensionless linear momentum range from p/M=0.095 to 0.75, while the incidence angles θ span from 6.36° to 2.83°. Initially, both BHs are non-spinning, as mentioned. Table I lists the number of simulations performed for each p/M, alongside with the corresponding ranges of incidence angles. We also provide fitted impact parameters, determined as explained in Appendix A.

TABLE I. Considered values of p/M along with their respective ranges of θ and the fitted ranges of impact parameters, b/M. The value N_S represents the number of simulations that have been computed for the given scenario.

p/M	θ (deg)	b/M	N_S
0.095	6.21 - 6.36	10.76 - 11.02	9
0.1225	5.04 - 5.14	8.76 - 8.91	10
0.245	3.29 - 3.32	5.71 - 5.77	12
0.3675	2.90 - 2.93	5.03 - 5.07	10
0.49	2.83 - 2.86	4.90 - 4.94	9
0.75	3.05 - 3.09	5.26 - 5.33	9

From Table I, we observe that the ranges of incidence angles and impact parameters that lead to capture become wider for smaller BH momenta. This is consistent with the expectation that slower-moving BHs require less precise alignment (i.e., larger θ) to undergo capture. Conversely, higher-momentum BHs require smaller impact parameters and incidence angles for capture. Interestingly, for the scenario with $p/M=0.75^1$, the range of incidence angles increases again; this peculiar behavior will be discussed in the next section.

In the following analysis, we study the evolution of BH properties throughout the interaction and after the merger, and characterize the corresponding GW signals. For quantities such as mass and spin, we focus on the post-merger regime, when these parameters reach stable asymptotic values (as indicated in previous works [4, 7], and as will be seen in the plateau parts of figures within Subsec. III A). For the GW analysis, we focus on the

¹ Analogously to [7], we use the term "case" to refer to a specific simulation with fixed initial conditions $\{p/M,\theta\}$, and the term "scenario" for the ensemble of cases corresponding to a given p/M.

regions of the signal where the Weyl scalar exhibits pronounced activity, examining the amplitude, frequency, and phase shift of each emission.

III. NUMERICAL RESULTS

A. General behavior of DCs

As discussed in the introduction, DCs behave similarly to CHEs, with the key difference being that the GW emission produced during the CHE is strong enough to bind the system, ultimately leading to a merger.

In Fig. 1 (upper panel), we show the Weyl scalar for a specific choice of p/M and θ , together with the trajectories of both BHs shown in the lower panel. Two distinct GW emissions are clearly visible: the first corresponds to the CHE, which binds the orbit, and the second to the final merger of the BHs. As seen in the lower panel, the initial close approach during the CHE produces a wide, temporary orbit lasting approximately 200M, followed by a nearly head-on merger.

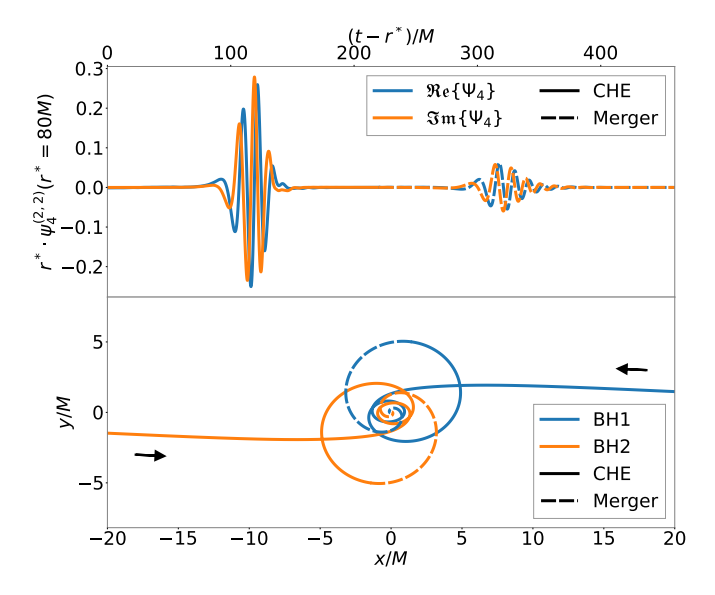


FIG. 1. (Upper panel) Evolution of the (2,2) multipole of the Weyl scalar measured at a detector located at a distance $r^* = 80M$ from the center of mass (CM). (Lower panel) Trajectories of both BHs, initially hyperbolic. The arrows qualitatively indicate the initial momentum \vec{p} of each BH. The solid and dashed lines roughly show when the BHs are in their CHE or merger phases, respectively. The initial conditions are p/M = 0.49, $\theta = 2.847^{\circ}$.

A relevant aspect to investigate in the following is how the initial conditions influence the amplitude and structure of these emissions. We expect that larger initial momenta lead to stronger GW emission during the CHE, since higher velocities imply more energetic and abrupt encounters with stronger frame-dragging effects. This trend is also tied to the impact parameter: higher values of p/M require smaller incidence angles to result in capture, thereby producing more intense GW bursts. This behavior will become clearer in the next section.

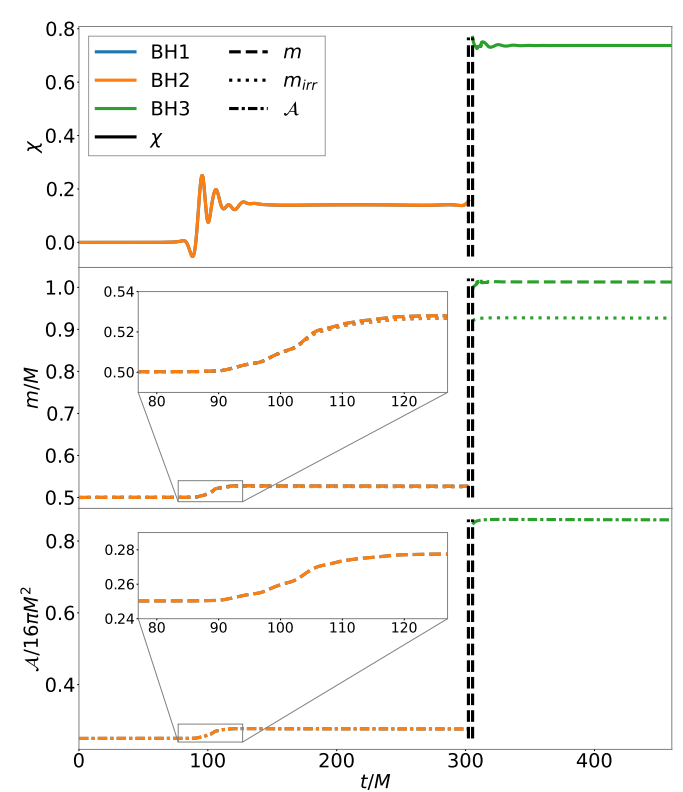


FIG. 2. (Upper panel) Evolution of the dimensionless spin parameter χ for each BH and for the final remnant. (Middle panel) Evolution of the ADM and irreducible masses of both BHs and of the merged remnant. (Lower panel) Evolution of the area \mathcal{A} for both BHs and the final one. Insets in the two lower panels are shown around the CHE phase. The initial conditions are $p/M=0.49,~\theta=2.847^{\circ}$. The black, vertical dashed lines indicate the moment of merger. Both BHs evolve in the same way, as their initial conditions are identical (see Subsec. II D).

In Fig. 2, we present the time evolution of the spin χ , ADM mass, and irreducible mass for each BH, as well as for the final remnant. Different colors are used to distinguish the final BH from the initial ones. Because we work in the center-of-mass frame with equal-mass BHs, both initial BHs evolve identically. During the CHE phase, there is a noticeable spin-up effect, consistent with previous findings for close hyperbolic interactions [4, 7].

In this example, the spin increases by approximately 0.14 during the CHE, while the ADM mass grows by about 5%. Both of these effects (tidal torquing and heating, respectively) are due to horizon absorption of backreacted GWs during the close encounter [42, 43]. Interestingly, the mass of the final BH slightly exceeds the combined pre-CHE masses of the two initial BHs, reaching about 1.01M. This shows that DCs can yield remnants with total mass greater than the initial sum, even after accounting for energy radiated away as GWs during

the merger.

Furthermore, the lower panel of Fig. 2 reveals that the horizon area of each BH also increases during the CHE. This is expected, since from Eq. (6) the area is directly related to the irreducible mass. The resulting remnant BH possesses an area larger than the sum of the progenitors, in accordance with Hawking's area law [44–46]. This behavior will be systematically verified for all simulations in Sec. IV.

As previously discussed in this work and in other studies [3, 4], DCs and pure CHEs exhibit qualitatively similar dynamics, with DCs ultimately leading to mergers that produce a second, prominent GW burst. This can also be visualized from the signal Q-plots, as shown in Appendix B. In the following section, we determine the critical incidence angle that marks the transition between the pure CHE regime and the DC regime.

B. Weyl scalar phenomenological model

Our next goal is to model the time evolution of the Weyl scalar Ψ_4 for each simulation. To do so, we adopt a simple two-stage fitting procedure:

• First emission (CHE phase): modeled as a *sin-Gaussian* function,

$$\Psi_4^{\rm E} = A_{\rm E} \sin \left[\omega_E (t - t_0^{\rm E}) + \phi_{\rm E} \right] e^{-\left(t - t_0^{\rm E}\right)^2 / 2\sigma_{\rm E}^2}, \quad (10)$$

applied to both the real and imaginary parts of Ψ_4 . The label "E" means emission in general, so to be explicit, the CHE parameters will be labeled "CHE".

• Second emission (merger and ringdown): divided into two components. The merger portion is described by an identical expression to Eq. (10) (with labels replaced by "M"), while the ringdown is modeled using the fundamental quasi-normal mode (n = 0) [47]:

$$\Psi_4^{\mathcal{R}} = \sum_n A_n^{\mathcal{R}} \sin\left[\omega_n^{\mathcal{R}}(t - t_a) + \phi_n^{\mathcal{R}}\right] e^{-(t - t_a)/\tau_n^{\mathcal{R}}}, \quad (11)$$

where t_a marks the transition between the merger and ringdown phases. These decaying modes appear as the final BH radiates away its distortions, settling into a stable Kerr BH state.

To ensure consistency and improve parameter accuracy, we first fit the amplitude envelope $\Psi_4 = \sqrt{\Psi_{4,R}^2 + \Psi_{4,I}^2}$ using a simple Gaussian profile, obtaining common values for $A_{\rm CHE}$, $t_0^{\rm CHE}$, and $\sigma_{\rm CHE}$ in the real and imaginary parts. A completely analogous approach is applied to the merger phase. This procedure assumes two physical conditions: (i) both real and imaginary parts share the same characteristic frequency, and

(ii) their phase shifts differ by $\pi/2$, as expected for a properly polarized GW signal.

Considering these conditions, once the amplitude-related parameters are determined, we perform a joint fit² of the real and imaginary parts, constraining them to share a common frequency and fulfilling the phase shift constraint

$$\phi_{E,R} = \phi_{E,I} - \frac{\pi}{2},$$
(12)

as mentioned before.

The ringdown portion of Ψ_4 is fitted in a similar fashion, but making use of the damped-sinusoid phenomenological model in Eq. (11), instead of the Gaussian function. Since we restrict the analysis to the dominant mode (n=0), the procedure remains tractable; including higher-order modes would require a more complex fitting scheme where the parameters of overlapping modes are not easily separable.

In Fig. 3, we show an example of the fitting results for the same case depicted in Figs. 1 and 2. The real and imaginary parts are shown separately, along with their fitted counterparts. The fits perform very well overall, particularly for the ringdown phase. The main discrepancies appear at the tails of the sin-Gaussian fits, likely due to the gradual variation of the orbital frequency over time. This is consistent with Kepler's law, where the gravitational-wave frequency obeys $\omega = 2\Omega$ [48], and the orbital separation evolves during each emission.

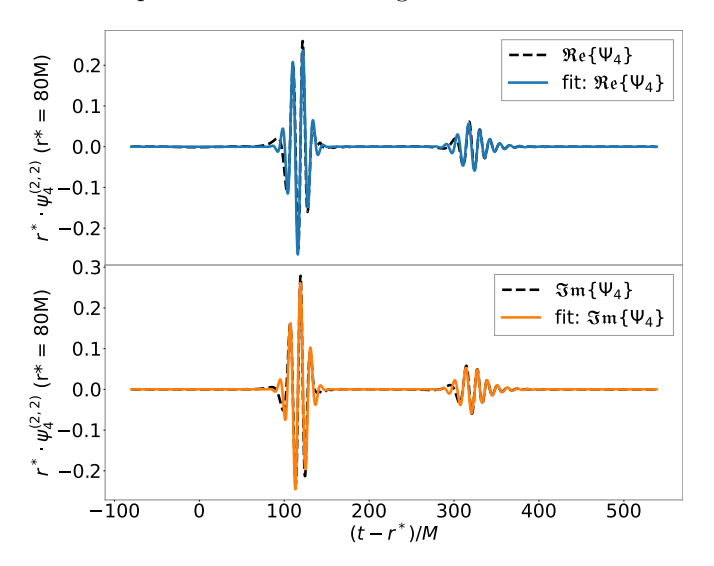


FIG. 3. Fits of the real (blue) and imaginary (orange) parts (upper and lower panels, respectively) compared to the simulated rescaled Weyl scalar (black dashed line) at a detector located at $r^* = 80M$ from the CM. The initial conditions correspond to the example case described in Sec. III A.

² For this, we concatenate the residues, and use least squares regression to minimize these to find a common frequency and phase shifts which fulfill Eq. (12).

C. Time-interval of gravitational-wave emissions

In this and the following subsections, we determine effective trends for each of the fitted parameters of the Weyl scalar in terms of the incidence angle (θ) . These relations will later serve as the basis for constructing a phenomenological model of DC waveforms. Before analyzing these dependencies, however, we first carry out the sin-Gaussian fits described previously and obtain a useful quantity that simplifies the discussion.

Using the parameters t_0^{CHE} and t_0^{M} (from Eq. (10)), we compute the temporal separation between the peaks of the two main emissions as

$$\Delta t \equiv t_0^{\rm M} - t_0^{\rm CHE}. \tag{13}$$

This quantity is physically meaningful: as the incidence angle increases, we approach the threshold value that separates pure CHEs (i.e. scattering events) from dynamical captures [3, 49]. In the limit where the interaction becomes a pure CHE, the merger never occurs, implying $\Delta t \to \infty$. Therefore, we expect a divergence in the trend of Δt as θ approaches this critical threshold angle θ_0 . This behavior is precisely what we observe in our simulations, as we show in the following.

In addition to determining the CHE/DC transition, another useful feature of θ_0 is that it allows us to "normalize" our horizontal axis when obtaining the trends of each parameter, leading to more compact and consistent visual representations despite the wide range of θ (and b/M) values explored in Tab. I.

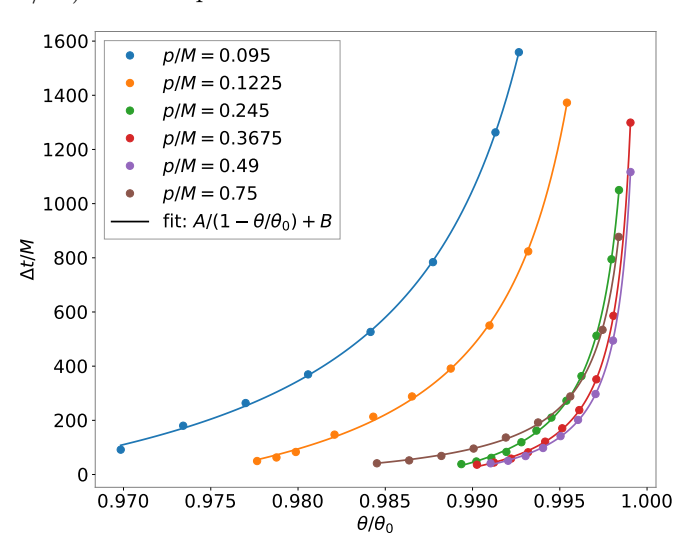


FIG. 4. Time intervals between peaks, $\Delta t = t_0^{\rm M} - t_0^{\rm CHE}$, as a function of the normalized incidence angle θ/θ_0 . The data points are obtained from the sin-Gaussian fits, while the solid curves (which diverge at $\theta/\theta_0 = 1$) represent fits using Eq. (14).

Figure 4 shows $\Delta t/M$ for each scenario, together with the best-fit function

$$\Delta t/M = \frac{A}{1 - \theta/\theta_0} + B,\tag{14}$$

whose parameters $(A, B, \text{ and } \theta_0)$ are listed in Tab. II.

TABLE II. Best-fit parameters obtained from Eq. (14). Uncertainties in parentheses correspond to 68% confidence-level errors on the last digit(s). The fitted curves are shown alongside the numerical data in Fig. 4.

p/M	$\theta_0 \text{ (deg)}$	A	В
0.095	6.404(1)	14.0(6)	-358(22)
0.1225	5.1629(7)	7.6(2)	-285(14)
0.245	3.3299(1)	1.92(4)	-147(6)
0.3675	2.93060(4)	1.33(2)	-108(3)
0.49	2.85889(4)	1.14(2)	-91(3)
0.75	3.0997(1)	1.51(3)	-56(4)

With this, we can now analyze the trend of θ_0 as a function of the initial momentum p/M. As discussed earlier (see Subsec. III A), higher momenta correspond to smaller threshold angles: the faster a black hole moves, the closer it must pass to the other to achieve capture. Interestingly, this monotonic behavior breaks down for the most relativistic cases $(p/M \gtrsim 0.49)$, where the threshold angle increases again. The extracted θ_0 values from Tab. II are plotted in Fig. 5.

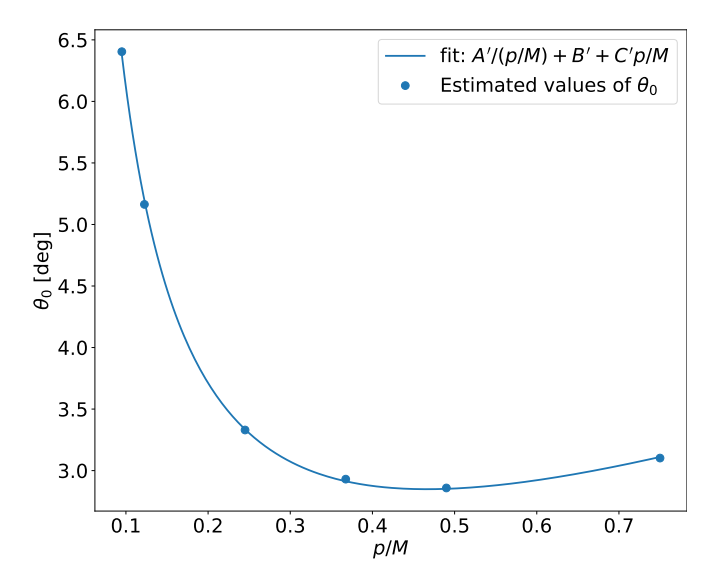


FIG. 5. Estimated threshold angles θ_0 (from Tab. II) as a function of the initial momentum p/M. The solid curve represents the best-fit model given by Eq. (15).

The best-fit model describing this relation is

$$\theta_0(p/M) = \frac{A'}{p/M} + B' + C'p/M,$$
 (15)

with coefficients A' = 0.529(6), B' = 0.58(6), and C' = 2.43(9) [deg] (1σ uncertainties shown in parentheses).

The observed upturn in θ_0 at large p/M remains physically unclear. A plausible explanation involves enhanced spin-orbit and spin-spin couplings at high velocities, since spin induction becomes significant for p/M > 0.3675. Following [7], the leading-order spin-spin Hamiltonian can be expressed as

$$H_{S_1S_2} \simeq -\frac{G}{c^2r^3} \Big(\vec{S}_1 \cdot \vec{S}_2 - 3(\vec{S}_1 \cdot \hat{\vec{r}}_1)(\vec{S}_2 \cdot \hat{\vec{r}}_2) \Big),$$
 (16)

where \vec{S}_j and \hat{r}_j denote the spin and unit position vector of each black hole (j=1,2), respectively. In this framework, parallel spins contribute negatively to the Hamiltonian, effectively increasing the attraction between the black holes. Thus, significant spin induction aligned with the orbital angular momentum (\vec{L}) facilitates the capture event, increasing θ_0 for larger p/M. Nevertheless, this remains speculative and requires further investigation.

D. Analysis and model of the CHE emission

We now focus on the fitted parameters describing the first (CHE) emission, as illustrated in Fig. 3. Depending on the observed behavior, we model these parameters using either a linear relation,

$$y = \alpha(\theta/\theta_0) + \beta,\tag{17}$$

or an exponential decay,

$$y' = \alpha \exp\{-\beta(1 - \theta/\theta_0)\} + \gamma, \tag{18}$$

where $y \in \{A_{\text{CHE}}, \omega_{\text{CHE}}, t_0^{\text{CHE}}\}$ and $y' \in \{\sigma_{\text{CHE}}, \phi_{\text{CHE,R}}, \phi_{\text{CHE,I}}\}.$

As shown in Fig. 6, the sin-Gaussian model describes the CHE emission with excellent accuracy, and the extracted parameters exhibit smooth and physically consistent trends. Two of them ($A_{\rm CHE}$ and $\omega_{\rm CHE}$) show slight deviations from strict linearity, suggesting mild non-linear dependencies that may carry physical meaning. Both parameters increase with θ/θ_0 up to a critical point and then change slope, likely reflecting that weaker GW bursts occur for larger incidence angles, while nearly head-on collisions also require less radiation to achieve capture.

The coefficients and uncertainties obtained from these fits are reported in Tab. IV, in the Appendix. Overall, this modeling strategy provides a robust and physically motivated description of the CHE waveform. Future refinements could address small discrepancies in the signal tails by considering time-dependent frequencies or expansions to higher-order modes.

Finally, we note that given the current sensitivity of the LVK detector network, the resulting phenomenological waveform model may already suffice for parameter estimation or signal detection of CHE events, which remain observationally elusive.

E. Analysis and model of the merger-ringdown emission

The final emission (the merger and ringdown) is modeled as two contiguous phases, ensuring continuity and differentiability between Eqs. (10) and (11) at the given transition time (t_a) . This time is chosen as $t_a = t_0 + 5M$, where t_0 corresponds to the maximum of the second emission (typically close to t_0^M).

1. Merger phase

The estimated parameters for the merger portion are summarized in Appendix C (see Fig. 10). Unlike the CHE case, no clear functional trends with θ/θ_0 were found, so we did not perform further fitting of the estimated parameters as was indeed done for the first emission in the previous subsection. There are three main factors which could explain this phenomenon:

- The estimated parameters for all scenarios (values of p/M) are of similar order of magnitude, leading to tightly clustered data points. This indicates that once a bound system forms after the CHE, the merger emits comparable amounts of energy and angular momentum regardless of the initial conditions.
- The division between merger and ringdown is somewhat arbitrary. The start of the ringdown occurs at slightly different times for the real and imaginary components, making the use of a single cutoff time (t_a) an approximation. In fact, there are entire works that tackle this concrete issue [50], and may be reason for further work.
- We use the entire merger-ringdown emission to estimate the parameters of the merger phase, which may be blurring the boundary between the two regimes. This choice was made because we checked that restricting the fit to only the rising portion of the peak worsens the results due to the strong non-linear dynamics present at this stage (and, especially as well, due to the small amount of sample points to estimate the necessary parameters).

Despite these issues, the fits perform reasonably well overall. The amplitude fit worsens particularly when both emissions (CHE and merger-ringdown) overlap significantly ($\Delta t/M \lesssim 100$), since the signals interfere nonlinearly at their tails (see an example of this in Fig. 13, in Appendix D). Conversely, the $t_0^{\rm M}$ parameter shows excellent agreement, as the fitted $\Delta t + t_0^{\rm CHE}$ values reproduce the simulated merger times remarkably well.

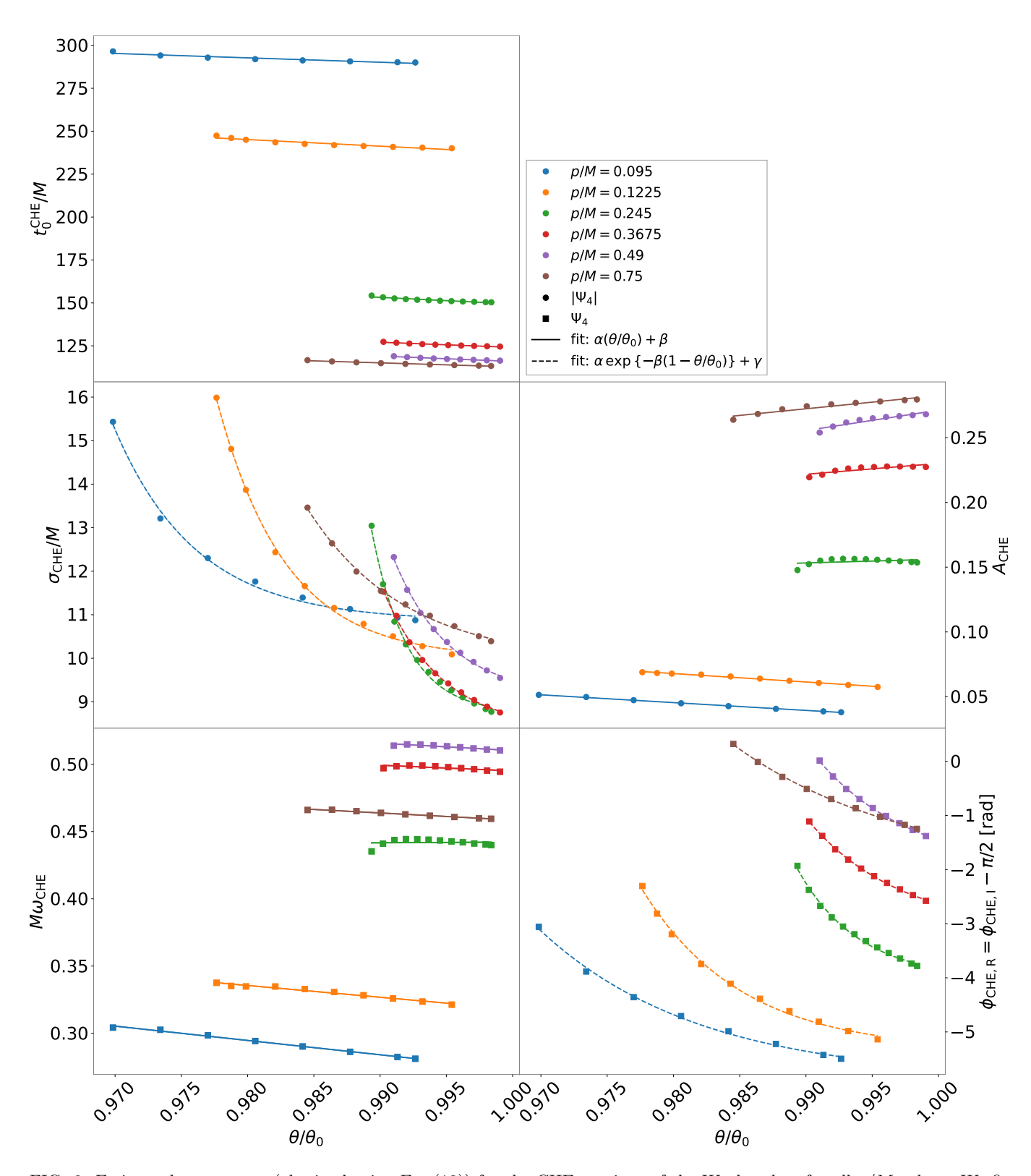


FIG. 6. Estimated parameters (obtained using Eq. (10)) for the CHE portions of the Weyl scalars for all p/M values. We fit these to linear fits (solid lines) which follow Eq. (17), and to exponential decays (dashed lines) which follow Eq. (18). Solid circles denote values obtained from the amplitude fit, while solid squares correspond to the sinusoid fit. The full set of fitted coefficients and their uncertainties is provided in Tab. IV. The values of the phase shifts have been extended to the range $(-2\pi, 2\pi]$ to properly study the observed trends.

2. Ringdown phase

The fits for the ringdown portion (see Fig. 11, in Appendix C) follow the same methodology as before: we first fit the amplitude, fix its value, and then fit the real and imaginary parts jointly (using Eq. (11)), enforcing a shared frequency and phase shifts following the constraint in Eq. (12). Although the fits reproduce the time evolution of the Weyl scalar quite accurately (as visually shown in Fig. 3), the fitted parameters themselves show mild oscillations and no analytical trends, particularly for smaller values of θ/θ_0 .

Future improvements will involve refining the cutoff time (t_a) that marks the start of the ringdown, potentially delaying it further to isolate the pure quasi-normal mode regime or applying techniques used in the literature [50], and improving the fits of the merger portion simultaneously.

While the current description already captures precise magnitudes of the relevant parameters, a more accurate treatment of the transition between merger and ringdown phases will be crucial for waveform modeling and GW data analysis applications.

IV. BLACK HOLE PROPERTIES

After analyzing the properties of the measured Weyl scalar, we now turn to the study of the intrinsic properties of the black holes (BHs): their spins and masses, as well as additional quantities derived from them. These quantities are computed using the QuasiLocalMeasures thorn of the Einstein Toolkit, as detailed in Subsec. II C.

All variables describing the final state of the BH are evaluated once the system reaches a relaxed configuration. For all cases, this time was chosen to be 140M after the merger.

For this section, we exclude the data corresponding to the most relativistic configuration, p/M=0.75. Although the associated waveforms are reliable, the final BHs obtained in these simulations present significant numerical uncertainties that prevent us from extracting physically meaningful results for their final states.

A. Analysis of spin

In Fig. 7 (upper left panel), we show the spin of the remnant BH measured at 140M after the merger for each case. The final spin lies within the range $\chi_{\rm f} \in [0.67, 0.77]$. We observe that the spin initially decreases with increasing θ/θ_0 , reaches a minimum (which varies slightly for each p/M), and then increases again. This nonmonotonic behavior can be interpreted similarly to the small deviations found in the parameters $(A_{\rm CHE}, \omega_{\rm CHE})$ discussed in Subsec. III D: for small θ/θ_0 , corresponding to near head-on collisions, the GW emission during the

CHE is weak (enough to bind the orbit but not significant enough to cause major energy or angular momentum losses). As θ/θ_0 increases, the emission becomes stronger, maximizing the energy and angular momentum loss and hence reducing the final spin. For even larger angles, the encounters become weaker again, leading to less GW emission and a corresponding increase in the final spin, as more angular momentum remains available to be converted into the spin of the remnant BH.

The rightmost red point in Fig. 7 deviates from the overall increasing trend, but this is likely due to numerical inaccuracies. Simulations at such large angles require longer evolution times, which accumulate significant numerical errors. This outlier will also affect the mass analysis later on.

It is also noticeable that the two lowest values of p/M yield nearly identical trends in their final spins. The green and red curves exhibit similar magnitudes to the blue and orange ones but develop a clearer positive slope beyond the critical point. The purple curve (p/M=0.49) differs most from the others, likely because higher p/M values induce stronger spins during the CHE phase, as reported in [3, 4]. For p/M=0.095-0.245, the merger occurs with negligible induced spin, leaving mainly the remnant orbital angular momentum to contribute to $\chi_{\rm f}$. In contrast, the p/M=0.49 case exhibits substantial induced spins ($\chi\sim0.14$) before the merger, leading to a higher final spin. The p/M=0.3675 case lies between these extremes, with induced spins of order $\chi\sim0.07$.

B. Analysis of the BH masses

In Subsec. IIB, we established the relation between ADM and irreducible masses (see Eq. (7)). These quantities are displayed in Fig. 7, where the middle left and middle right panels show $M_{\rm f}$ and $M_{\rm f,irr}$, respectively.

In the upper right panel of Fig. 7, we plot the extractable energy (defined as $E_{\rm extractable} \equiv M_{\rm f} - M_{\rm f,irr}$) which represents the maximum amount of energy that can be extracted from a Kerr BH through processes such as the Penrose mechanism or BH mergers [24]. In the upper panels of this figure, one can see that the trends of $E_{\rm extractable}$ closely follow those of $\chi_{\rm f}$, suggesting a strong direct dependence between both quantities. This can be explained by expanding the irreducible mass formula,

$$M_{\rm irr,f} = M_{\rm f} \sqrt{\frac{1 + \sqrt{1 - \chi_{\rm f}^2}}{2}},$$
 (19)

around $\chi_f = 0.686$, for reference (the typical final spin for quasicircular mergers). With this, we obtain

$$\frac{E_{\text{extractable,f}}}{M_{\text{f}}} \approx 0.071 + 0.235(\chi_{\text{f}} - 0.686),$$
 (20)

which explains the almost linear correlation observed between the extractable energy and the final spin, as our

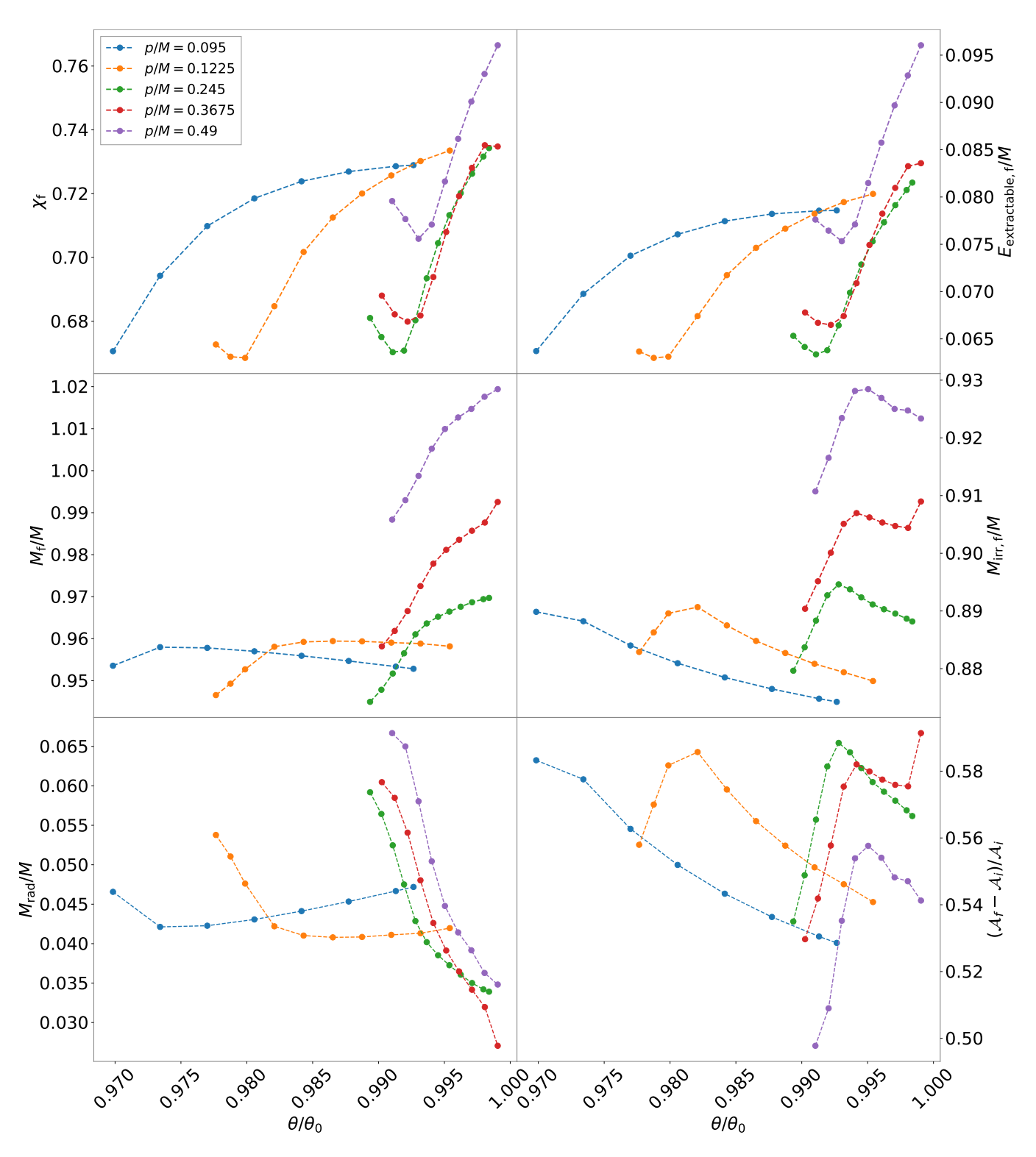


FIG. 7. Spin (upper left panel), extractable energy (upper right panel), mass (middle left panel) and irreducible mass (middle right panel) of the final BH as functions of the normalized angle θ/θ_0 for each scenario. With respect to the same variable in the horizontal axis, we show the total radiated mass (lower left panel) when the BHs merge and the fractional area difference (lower right panel) between the final BH and the ones before the merger. Final values have been computed at a time of 140M after the merger, while values prior to the merger (and after the CHE) have been calculated at a time 30M before the coalescence.

results remain close to $\chi_{\rm f}=0.686,$ making the linear approximation valid.

The extractable energy varies within $E_{\rm extractable} \in [0.064, 0.097]$, with the largest values corresponding to the most relativistic encounters (p/M=0.49), which exhibit the highest induced spins and therefore the greatest potential for energy extraction.

Additionally, in the middle left panel of Fig. 7, we observe that the final mass generally increases with θ/θ_0 , particularly for p/M=0.3675 and p/M=0.49. For smaller p/M values, the slope changes sign near the critical point: the orange curve flattens, while the blue one turns slightly negative. The origin of this transition is not entirely clear; it likely reflects the interplay between GW emission, spin induction, and mass increase.

Future work should focus on quantifying the correlations between spin, ADM mass, and irreducible mass (which consistently show a negative slope beyond the critical point) to better understand the underlying mechanisms. Effects such as angular momentum redistribution, tidal torquing, and tidal heating through horizon absorption³ all likely contribute to the complex trends observed in these simulations of dynamical captures [42, 51]. In future works, we also plan to compare the obtained final spins and masses with those predicted for quasicircular and head-on mergers with equivalent effective spins, expecting our results to lie between these limiting cases.

C. Analysis of radiated mass and BH areas

Finally, we evaluate the radiated mass during the merger. When two BHs coalesce, they emit large amounts of energy and angular momentum as gravitational waves. The remaining angular momentum contributes to the final spin, while part of the emitted energy corresponds to a loss in total mass. Consequently, the mass of the final BH is smaller than the combined mass of the progenitors, allowing us to define the radiated mass for an equal-mass system as:

$$M_{\rm rad} = 2m - M_{\rm f}. \tag{21}$$

Here, m is the mass of one of the BHs before the merger. Because of horizon absorption, in general $2m \neq M$, where M is the total initial mass of the system. To properly account for this, we evaluate m at a time 30M before the merger.

The results are shown in the lower left panel of Fig. 7, where we find that more head-on collisions emit more mass as GW radiation, and that more relativistic encounters radiate a larger fraction of the total mass. These

mergers radiate roughly between 3% and 6% of the total initial mass as GWs; a range consistent with typical LVK observations (for instance, GW150914 radiated about 4.6% of its total mass [52, 53]).

Future detections may reveal events with even higher radiated mass percentages (8% - 10%), potentially signaling highly relativistic BH encounters ($p/M \gg 0.49$) on nearly head-on trajectories; a distinctive signature of dynamical capture.

Lastly, we analyze the change in horizon area. According to Hawking's area theorem, the total BH area cannot decrease over time through classical processes, implying $\mathcal{A}_f > \mathcal{A}_i = \mathcal{A}_{1,i} + \mathcal{A}_{2,i}$. This was recently confirmed using ringdown measurements [45]. Using the QuasiLocalMeasures thorn, we can directly compute these areas before and after merger. Figure 7 shows that all our simulations satisfy this condition, in full agreement with Hawking's area law.

V. CONCLUSIONS

In this paper, we have presented a first comprehensive approach to the analysis of dynamical captures (DCs) that culminate in a merger. Our primary objective was to model the outgoing gravitational radiation of such events and to study the trends of the spins, masses, and irreducible masses of the final black holes as functions of the incidence angle.

Using the waveform-fitting procedure described throughout this work, we obtained an accurate parametrization of the time separation between the close hyperbolic encounter and the merger-ringdown emissions $(\Delta t/M)$, as shown in Eq. (4). This characterization allowed us to define the threshold angle θ_0 , which marks the transition between purely scattering encounters and dynamical captures.

Furthermore, as discussed in Subsec. III D, the sin-Gaussian parametrization introduced in Eq. (10) reproduces the Weyl scalar with remarkable precision. The fitted parameters exhibit clear and consistent trends with respect to the normalized incidence angle θ/θ_0 , indicating that this model captures the essential physical features of the CHE emission phase.

In contrast, the parameters describing the merger and ringdown emissions display less regular behavior, as seen in Appendix C. Some of these quantities, particularly the phase shifts, show mild oscillations or clustering around similar orders of magnitude, complicating the identification of global trends using analytical functions. Nevertheless, the model described in Subsec. III E (Eqs. (10) and (11)) achieves good overall agreement with the NR Weyl scalar (see Fig. 3), providing a robust phenomenological description of the characteristic frequencies, amplitudes, and timescales that shape the final emission.

Additionally, Fig. 7 illustrates the dependencies of the final black hole spin, extractable energy, ADM mass, irreducible mass, radiated energy, and fractional

 $^{^3}$ Horizon absorption can explain why $M_{\rm f}$ exceeds 1M in some cases (see the middle left panel of Fig. 7), since after the CHE the individual masses can reach $m/M \sim 0.52,$ thus increasing the total ADM mass.

area difference on θ/θ_0 across different initial conditions. These results highlight the complex interplay between gravitational-wave emission, initial angular momentum, and relativistic mechanisms such as spin induction [3, 4, 7] and horizon absorption (tidal heating and torquing) [42, 43]. A deeper understanding of these effects will be crucial to fully interpret the observed behaviors and to refine future models of dynamical-capture phenomenology.

In conclusion, this paper lays the groundwork for the development of a comprehensive waveform model for dynamical captures. Such a model will not only improve our understanding of the waveform morphology, but also provide insights into the underlying orbital dynamics, spin interactions, and mass-energy exchange mechanisms that govern these extreme events. Future work will focus on extending and refining this framework, ultimately leading to a more complete picture of CHEs and DCs, and perhaps also studying whether these events occur as well for neutron stars [54]. As detector sensitivities continue to improve, these results are expected to play an important role in the potential detection and interpretation of GW signals from dynamical capture events.

ACKNOWLEDGMENTS

All the simulations have been run in the Hydra HPC cluster at the IFT. JGB acknowledges support from the Spanish Research Project PID2021-123012NB-C43 [MICINN-FEDER], and the Centro de Excelencia Severo Ochoa Program CEX2020-001007-S at IFT. SJ acknowledges support from the Agence Nationale de la Recherche (ANR) under contract ANR-22-CE31-0001-01.

Appendix A: Impact parameters estimated from the black hole trajectories

After the initial conditions stabilize, and before the black holes interact, we can fit their trajectories to hyperbolic-like curves. We choose to fit the part of the trajectory corresponding to the times 30-38M. From these hyperbolae, one can get the value of the impact parameter of each case.

Since we are in a regime of small angles (see Tab. I), we expect that the trend followed by the impact parameters with respect to the incidence angle is linear. This can be seen in Fig. 8, where we have included a linear fit (Eq. 17) for the estimated impact parameters.

We can check that indeed, in the fits of the estimated impact parameters, $\beta \approx 0$ (see Tab. III), which implies that we recover the small-angle approximation for the impact parameter, $b/M \approx \alpha\theta/\theta_0$, showing that DCs occur within this regime of small incidence angles (or impact parameters).

In fact, we have can easily see that $\alpha/\theta_0 \approx 100$, as one would expect from the setup described in Sub-

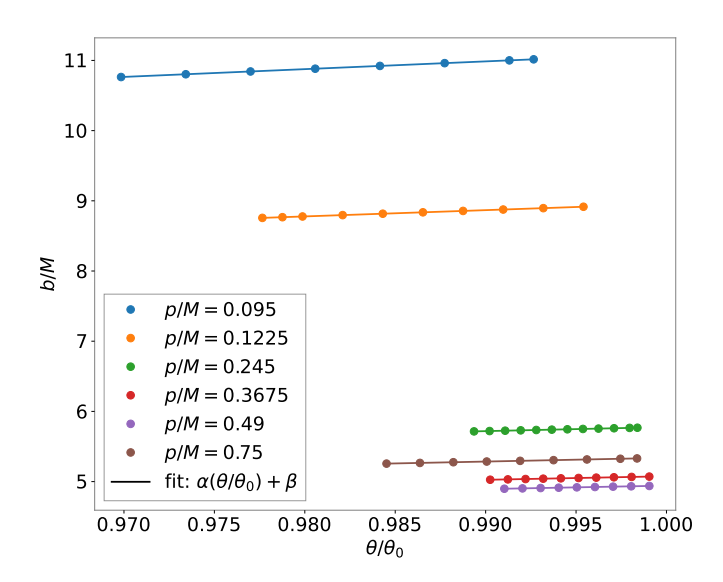


FIG. 8. Estimated impact parameters (b/M) in terms of the normalized incidence angle θ/θ_0 for each scenario.

TABLE III. Best-fit parameters obtained from Eq. (17) for the estimated impact parameters. Uncertainties in parentheses correspond to 68% confidence-level errors on the last digit(s). The fitted curves are shown alongside the numerical data in Fig. 8.

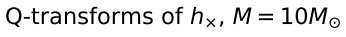
p/M	α	β	
0.095	11.0539(2)	0.0428(2)	
0.1225	8.9343(4)	0.0221(4)	
0.245	5.773(2)	0.003(1)	
0.3675	5.0740(5)	0.0021(4)	
0.49	4.9408(5)	0.0018(5)	
0.75	5.3358(6)	0.0029(5)	

sec. II D. However, the analogous value of the threshold incidence angle for the impact parameter is properly obtained (within this framework) as $b_0/M = \alpha + \beta$.

Appendix B: Examples of Q-transforms

In the context of GW detection, it is common to visualize GW signals through spectrograms, also called Q-plots [52, 53]. Therefore, as visual illustrations of these for DCs; in Fig. 9 we show four examples (using an initial total mass of $10M_{\odot}$) of Q-plots for the cross polarization of the simulated strain (h_{\times}). We see that larger incidence angles separate the peaks, as expected from our analysis. Additionally, it can be noted that when increasing the incidence angle, the intensity of the second emission starts growing, while the one of the first emission diminishes.

In these plots, we can also see that the CHE emis-



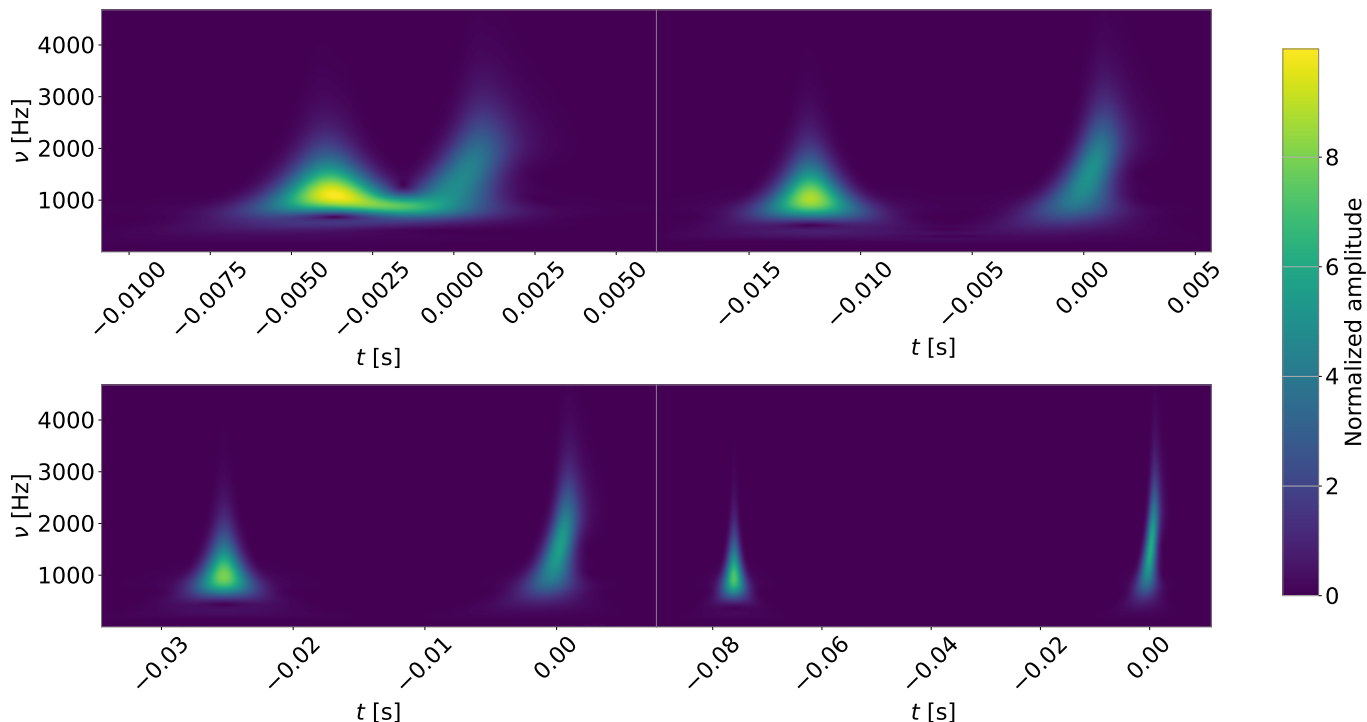


FIG. 9. Example of Q-transforms over the cross polarization (h_{\times}) of the strain from NR simulations with p/M=0.095. The angles of incidence (from left to right and from top to bottom) are: $\theta=6.21,\,6.26,\,6.30,\,6.36^{\circ}$. The chosen initial total mass is $M=10M_{\odot}$. For these spectrograms, we mark t=0 as the merger time.

sion is produced in a chirp-like form, which is a desired result for this type of emissions [6]. In the upper left plot, we see evidently that when the incidence angle is sufficiently small to create a DC where both emissions have short time-intervals in between, both the merger and CHE portions of the Q-plot fuse together, creating a complex behavior that cannot be accurately described. This makes even more evident cause of the oscillations in the estimated parameters for smaller θ/θ_0 in Figs. 10 and 11, especially in the phase shift, as explained in the following section of the Appendix.

Appendix C: Figures of estimated parameters for the Merger and Ringdown

In this section, we show the obtained parameters for the merger emission of each case (Fig. 10). The procedure is explained in full detail in Subsec. III E. We can see that general trends can be seen (especially for t_0^M , $A_{\rm M}$ and $\omega_{\rm M}$), but there is room for improvement. This is especially evident for the phase shifts, more specifically, for low θ/θ_0 in each scenario, where oscillations appear and no clear trends can be deduced. A very similar phenomenon occurs for the estimated ringdown parameters (Fig. 11), where oscillations come at play once again.

As no clear trends have been found in this work, we have not carried out any fits to the parameters. We will

attempt to obtain clearer trends in future works, as well as fitting the different parameters with respect to θ/θ_0 , as it was done for the CHE case in Subsec. III D, with Eqs. (17) and. (18). Nevertheless, this study helps us see the orders of magnitude that the GW emissions in DC events have, paving the way towards a future DC waveform model.

Furthermore, in Fig. 12, we plot the ratio $A_{\rm M}/A_{\rm CHE}$, which shows us that the least relativistic scenarios presented in this work have merger amplitudes ranging from about the order of the CHE emission to twice as large. Meanwhile, the most relativistic scenarios present CHEs much stronger, reaching values of CHE amplitudes four or five times larger than that of the merger.

Appendix D: An example of the overlap of the tails of both emissions

In Fig. 13, we show the performance of the combination of fits described in Sec. IIIB for a case where the tails of both sin-Gaussian distributions combine with each other. This is the main reason we observe the oscillations for the merger-ringdown estimated parameters (especially the phase shifts) in Figs. 10 and 11.

These issues we observe at the tails for emissions with small time-interval might be potentially fixed by a time-dependent frequence or expansion of Eqs. (10) and (11)

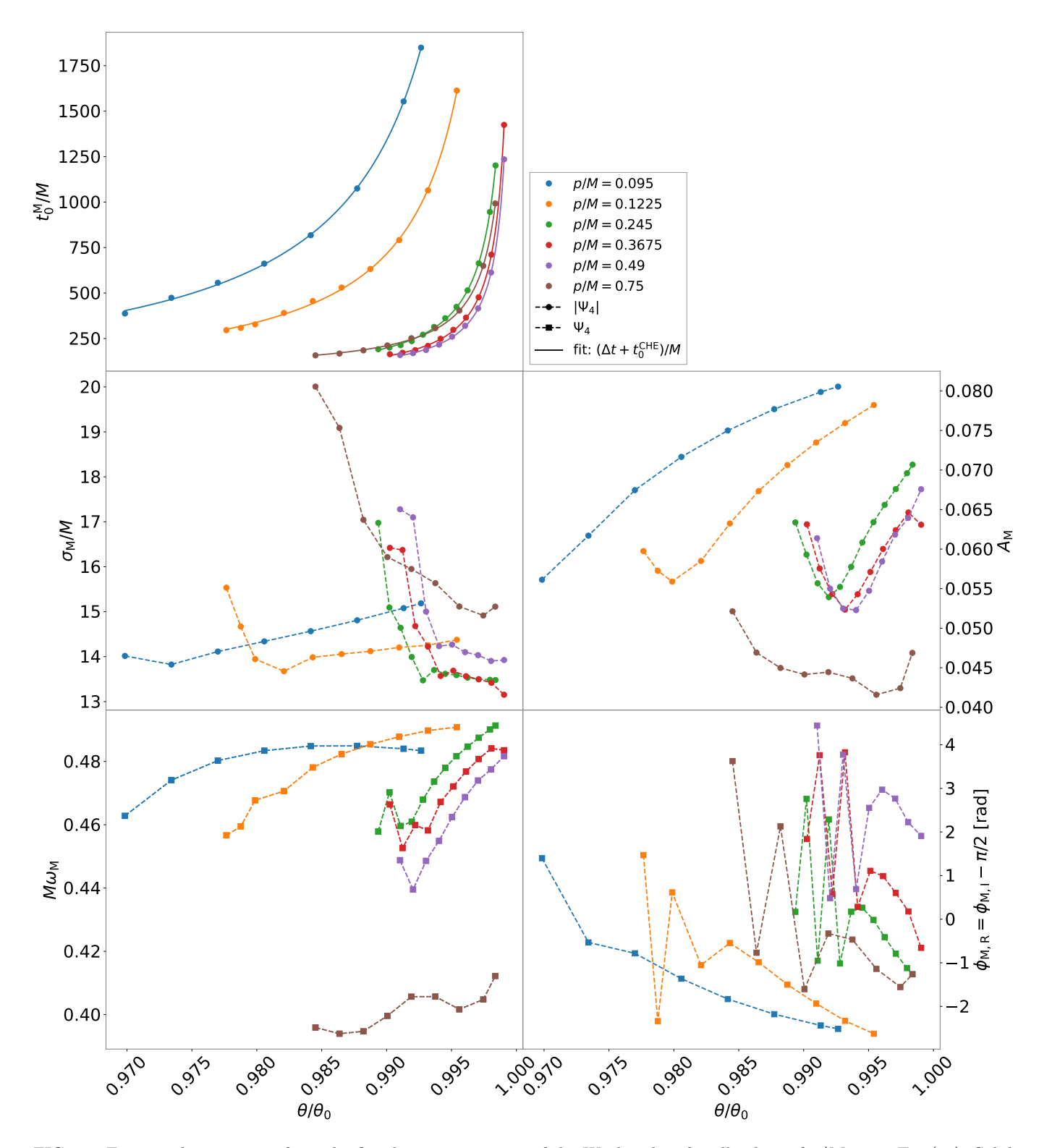


FIG. 10. Estimated parameters from the fitted merger portions of the Weyl scalars for all values of p/M using Eq. (10). Solid circles denote values obtained from the amplitude fit, while solid squares correspond to the sinusoid fit. Following the procedure shown in Fig. 6, the range of phase shifts has been extended to the range $(-2\pi, 2\pi]$.

TABLE IV. Calculated fitting values with respect to θ/θ_0 for the estimated parameters of the CHE portion of the Weyl scalar according to the methodology described in Sec. III D. In particular, the types of fits we use for each parameter are either "Linear" or "Exponential" (see Eqs. (17) and (18)). For the phase shift, only $\phi_{\text{CHE},I}$ is shown because we have imposed the physical constraint in Eq. (12), making $\phi_{\text{CHE},I}$ easily computable. Other parameters are identical for the real and imaginary parts, as throughly explained in Subsec. III B. The uncertainties of the estimated coefficients are written on the last digits(s) at 1σ in parentheses.

CHE Parameter	Fit	p/M	α	β	γ
A_{CHE}	Linear	0.095	-0.60(1)	0.635(9)	_
		0.1225	-0.65(2)	0.70(2)	_
		0.245	0.3(2)	0.1(2)	_
		0.3675	0.8(2)	-0.6(2)	_
		0.49	1.5(2)	-1.30(2)	_
		0.75	1.0(1)	-0.7(1)	_
	Exponential	0.095	0.03(1)	162(12)	10.8(9)
		0.1225	0.08(1)	192(7)	9.99(7)
		0.245	0.08(2)	370(23)	8.73(7)
$\sigma_{ m CHE}$		0.3675	0.35(4)	226(11)	8.34(7)
		0.49	0.37(6)	238(16)	9.13(9)
		0.75	0.42(7)	136(9)	9.9(1)
		0.095	-255(30)	543(29)	_
	Linear	0.1225	-384(42)	621(34)	_
$t_0^{ m CHE}$		0.245	-382(34)	531(33)	_
t_0		0.3675	-302(19)	426(19)	_
		0.49	-313(17)	429(18)	_
		0.75	-231(12)	344(13)	_
	Linear	0.095	-1.06(3)	1.33(3)	_
		0.1225	-0.87(4)	1.19(4)	
4.1		0.245	0.05(26)	0.4(2)	_
$\omega_{ m CHE}$		0.3675	-0.41(4)	0.91(3)	_
		0.49	-0.54(8)	1.05(8)	_
		0.75	-0.52(2)	0.98(2)	_
	Exponential	0.095	0.22(5)	82(7)	-5.9(1)
		0.1225	0.15(3)	132(10)	-5.35(9)
d		0.245	0.20(4)	215(18)	-4.03(7)
$\phi_{\mathrm{CHE,R}}$		0.3675	0.51(4)	141(7)	-3.14(5)
		0.49	0.59(7)	138(9)	-2.04(8)
		0.75	0.73(9)	75(5)	-2.0(1)

at higher-order modes, and may be a possible source of future work for refining this phenomenological model.

REFERENCES

- J. García-Bellido and S. Nesseris, Phys. Dark Univ. 18, 123 (2017), arXiv:1706.02111 [astro-ph.CO].
- [2] J. García-Bellido and S. Nesseris, Phys. Dark Univ. 21, 61 (2018), arXiv:1711.09702 [astro-ph.HE].
- [3] P. E. Nelson, Z. B. Etienne, S. T. McWilliams,

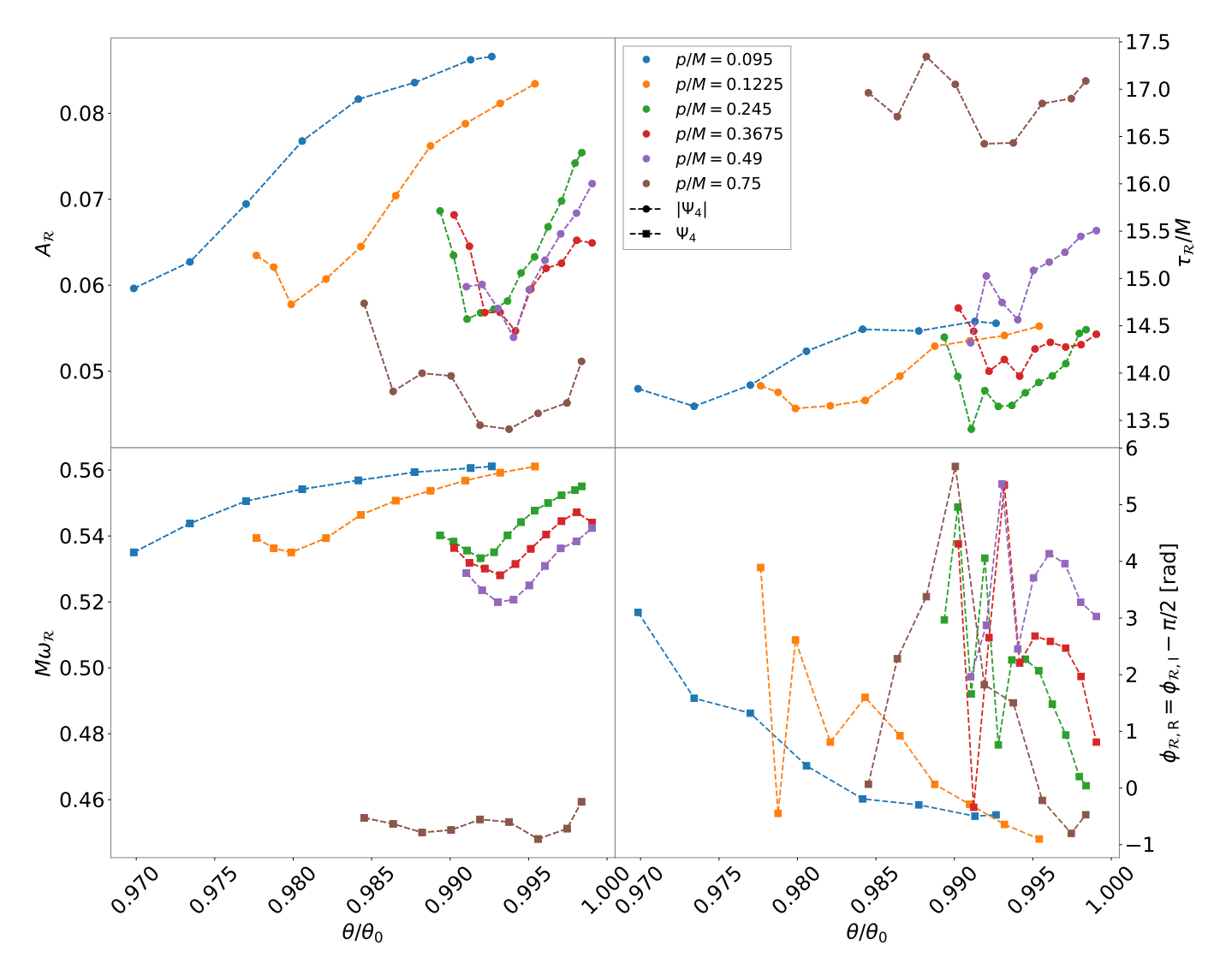


FIG. 11. Estimated parameters of the first mode of the ringdown portion of the Weyl scalars for all values of p/M using Eq. (11). Solid circles denote values obtained from the amplitude fit, while solid squares correspond to the sinusoid fit. Following the procedure shown in Fig. 6, the range of phase shifts has been extended to the range $(-2\pi, 2\pi]$.

- and V. Nguyen, Phys. Rev. D 100, 124045 (2019), arXiv:1909.08621 [gr-qc].
- [4] S. Jaraba and J. García-Bellido, Phys. Dark Univ. ${\bf 34},$ 100882~(2021), arXiv:2106.01436 [gr-qc].
- [5] J. García-Bellido, S. Jaraba, and S. Kuroyanagi, Phys. Dark Univ. 36, 101009 (2022), arXiv:2109.11376 [gr-qc].
- [6] G. Morrás, J. García-Bellido, and S. Nesseris, Phys. Dark Univ. 35, 100932 (2022), arXiv:2110.08000 [astro-ph.HE].
- [7] J. L. Rodríguez-Monteverde, S. Jaraba, and J. García-Bellido, Phys. Dark Univ. 47, 101776 (2025), arXiv:2410.11634 [gr-qc].
- [8] J. Fontbuté, T. Andrade, R. Luna, J. Calderón Bustillo, G. Morrás, S. Jaraba, J. García-Bellido, and G. L. Izquierdo, Phys. Rev. D 111, 044024 (2025), arXiv:2409.16742 [gr-qc].
- [9] A. Nagar, P. Rettegno, R. Gamba, and S. Bernuzzi, Phys. Rev. D 103, 064013 (2021), arXiv:2009.12857 [gr-qc].

- [10] S. Albanesi, A. Rashti, F. Zappa, R. Gamba, W. Cook, B. Daszuta, S. Bernuzzi, A. Nagar, and D. Radice, Phys. Rev. D 111, 024069 (2025), arXiv:2405.20398 [gr-qc].
- [11] J. Trenado, T. Andrade, A. Climent, and M. A. Ferrer, "First ICCUB Numerical Relativity Waveform Catalog of Eccentric Black Hole Binaries," (2025), arXiv:2509.05269 [gr-qc].
- [12] J. F. N. Siles and J. García-Bellido Capdevila, Phys. Dark Univ. 47, 101789 (2025), arXiv:2405.06391 [astro-ph.CO].
- [13] J. Aasi et al. (LIGO Scientific), Class. Quant. Grav. 32, 074001 (2015), arXiv:1411.4547 [gr-qc].
- [14] F. Acernese et al. (VIRGO), Class. Quant. Grav. 32, 024001 (2015), arXiv:1408.3978 [gr-qc].
- [15] T. Akutsu et al. (KAGRA), PTEP 2021, 05A101 (2021), arXiv:2005.05574 [physics.ins-det].
- [16] R. M. O'Leary, Y. Meiron, and B. Kocsis, Astrophys. J. Lett. 824, L12 (2016), arXiv:1602.02809 [astro-ph.HE].
- [17] B. Liu and V. Bromm, Mon. Not. Roy. Astron. Soc. 495,

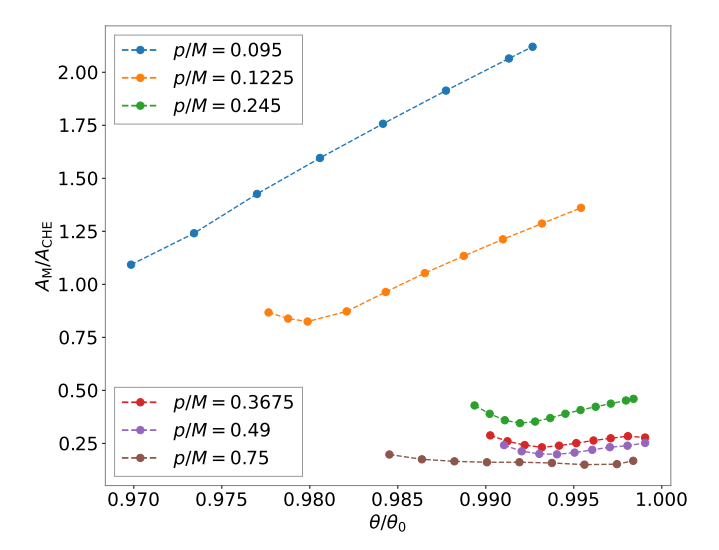


FIG. 12. Ratio of the estimated amplitudes for the merger and CHE emissions $(A_{\rm M}/A_{\rm CHE})$, obtained using Eq. (10). These values have been separately shown in their respective Figs. 10 and 6.

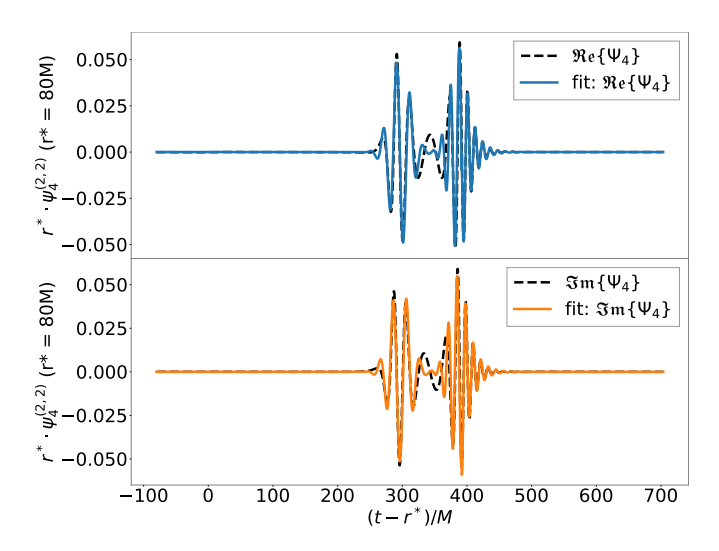


FIG. 13. Fits of the real (blue) and imaginary (orange) parts (upper and lower panel respectively) along with the simulated signal (black, dashed) of the rescaled Weyl scalar at a detector at a distance $r^* = 80M$ from the CM. The initial conditions are p/M = 0.095 and $\theta = 6.2108^{\circ}$, with zero initial spins.

- 2475 (2020), arXiv:2003.00065 [astro-ph.CO].
- [18] R. Gamba, M. Breschi, G. Carullo, S. Albanesi, P. Rettegno, S. Bernuzzi, and A. Nagar, Nature Astronomy 7, 11–17 (2022).
- [19] T. Chiba and S. Yokoyama, Progress of Theoretical and Experimental Physics 2017 (2017), 10.1093/ptep/ptx087.
- [20] E. Newman and R. Penrose, J. Math. Phys. 3, 566 (1962).
- [21] M. Maggiore, Gravitational Waves. Vol. 2: Astrophysics and Cosmology (Oxford University Press, 2018).
- [22] E. Altas and B. Tekin, Journal of Physics: Conference Series 2191, 012002 (2022).
- [23] S. R. Brandt and E. Seidel, Physical Review D 54,

- 1403-1416 (1996).
- [24] R. Ruffini, C. L. Bianco, M. Prakapenia, H. Quevedo, J. A. Rueda, and S. R. Zhang, "The role of the irreducible mass in repetitive penrose energy extraction processes in a kerr black hole," (2024), arXiv:2405.10459 [gr-qc].
- 25] M. Alcubierre et al., Phys. Rev. D **72**, 044004 (2005).
- [26] D. Gerosa and Others, Phys. Rev. D 108, 024042 (2023).
- [27] O. Dreyer, B. Krishnan, D. Shoemaker, and E. Schnetter, Phys. Rev. D 67, 024018 (2003), arXiv:gr-qc/0206008.
- [28] F. Loffler et al., Class. Quant. Grav. 29, 115001 (2012), arXiv:1111.3344 [gr-qc].
- [29] "Einstein Toolkit: Open software for relativistic astrophysics," https://www.einsteintoolkit.org/.
- [30] T. Goodale, G. Allen, G. Lanfermann, J. Massó, T. Radke, E. Seidel, and J. Shalf, in Vector and Parallel Processing – VECPAR'2002, 5th International Conference, Lecture Notes in Computer Science (Springer, Berlin, 2003).
- [31] Cactus developers, "Cactus Computational Toolkit," http://www.cactuscode.org/.
- [32] E. Schnetter, S. H. Hawley, and I. Hawke, Class. Quantum Grav. 21, 1465 (2004), arXiv:gr-qc/0310042.
- [33] "Carpet: Adaptive mesh refinement for the Cactus framework," https://bitbucket.org/eschnett/carpet.git.
- [34] M. Ansorg, B. Bruegmann, and W. Tichy, Phys. Rev. D 70, 064011 (2004), arXiv:gr-qc/0404056.
- [35] V. Paschalidis, Z. B. Etienne, R. Gold, and S. L. Shapiro, "An efficient spectral interpolation routine for the TwoP-unctures code," (2013), arXiv:1304.0457 [gr-qc].
- [36] J. D. Brown, P. Diener, O. Sarbach, E. Schnetter, and M. Tiglio, Phys. Rev. D 79, 044023 (2009), arXiv:0809.3533 [gr-qc].
- [37] Kranc, "Kranc assembles numerical code," http:// kranccode.org/.
- [38] McLachlan, "McLachlan, a public BSSN code," http://www.cct.lsu.edu/~eschnett/McLachlan/.
- [39] J. Thornburg, Class. Quant. Grav. 21, 743 (2004), arXiv:gr-qc/0306056.
- [40] J. Thornburg, Phys. Rev. D 54, 4899 (1996), arXiv:gr-qc/9508014.
- [41] M. Zilhão and F. Löffler, Int. J. Mod. Phys. A 28, 1340014 (2013), arXiv:1305.5299 [gr-qc].
- [42] D. Chiaramello and R. Gamba, Phys. Rev. D 111, 024024 (2025), arXiv:2408.15322 [gr-qc].
- [43] C. Munna, C. R. Evans, and E. Forseth, Phys. Rev. D 108, 044039 (2023).
- [44] S. W. Hawking, Phys. Rev. Lett. 26, 1344 (1971).
- [45] A. G. Abac et al. (KAGRA, Virgo, LIGO Scientific), Phys. Rev. Lett. 135, 111403 (2025), arXiv:2509.08054 [gr-qc].
- [46] D. Christodoulou, Phys. Rev. Lett. 25, 1596 (1970).
- [47] J. Redondo-Yuste, D. Pereñiguez, and V. Cardoso, Phys. Rev. D 109, 044048 (2024), arXiv:2312.04633 [gr-qc].
- [48] M. Maggiore, Gravitational Waves: Volume 1: Theory and Experiments (Oxford University Press, 2007).
- [49] P. Rettegno, G. Pratten, L. M. Thomas, P. Schmidt, and T. Damour, Phys. Rev. D 108, 124016 (2023), arXiv:2307.06999 [gr-qc].
- [50] S. Bhagwat, M. Okounkova, S. W. Ballmer, D. A. Brown, M. Giesler, M. A. Scheel, and S. A. Teukolsky, Physical Review D 97 (2018), 10.1103/physrevd.97.104065.

- [51] K. Chatziioannou, E. Poisson, and N. Yunes, Phys. Rev. D $\bf 87,\,044022$ (2013).
- [52] B. P. Abbott et al. (LIGO Scientific Collaboration and Virgo Collaboration), Phys. Rev. Lett. 116, 061102 (2016).
- [53] R. Abbott et al. (LIGO Scientific Collaboration, Virgo
- Collaboration, and KAGRA Collaboration), Phys. Rev. X ${\bf 13},\,041039$ (2023).
- [54] J. Fontbuté, S. Bernuzzi, P. Rettegno, S. Albanesi, and W. Tichy, "Gravitational scattering of two neutron stars," (2025), arXiv:2506.11204 [gr-qc].